

Figure 1.

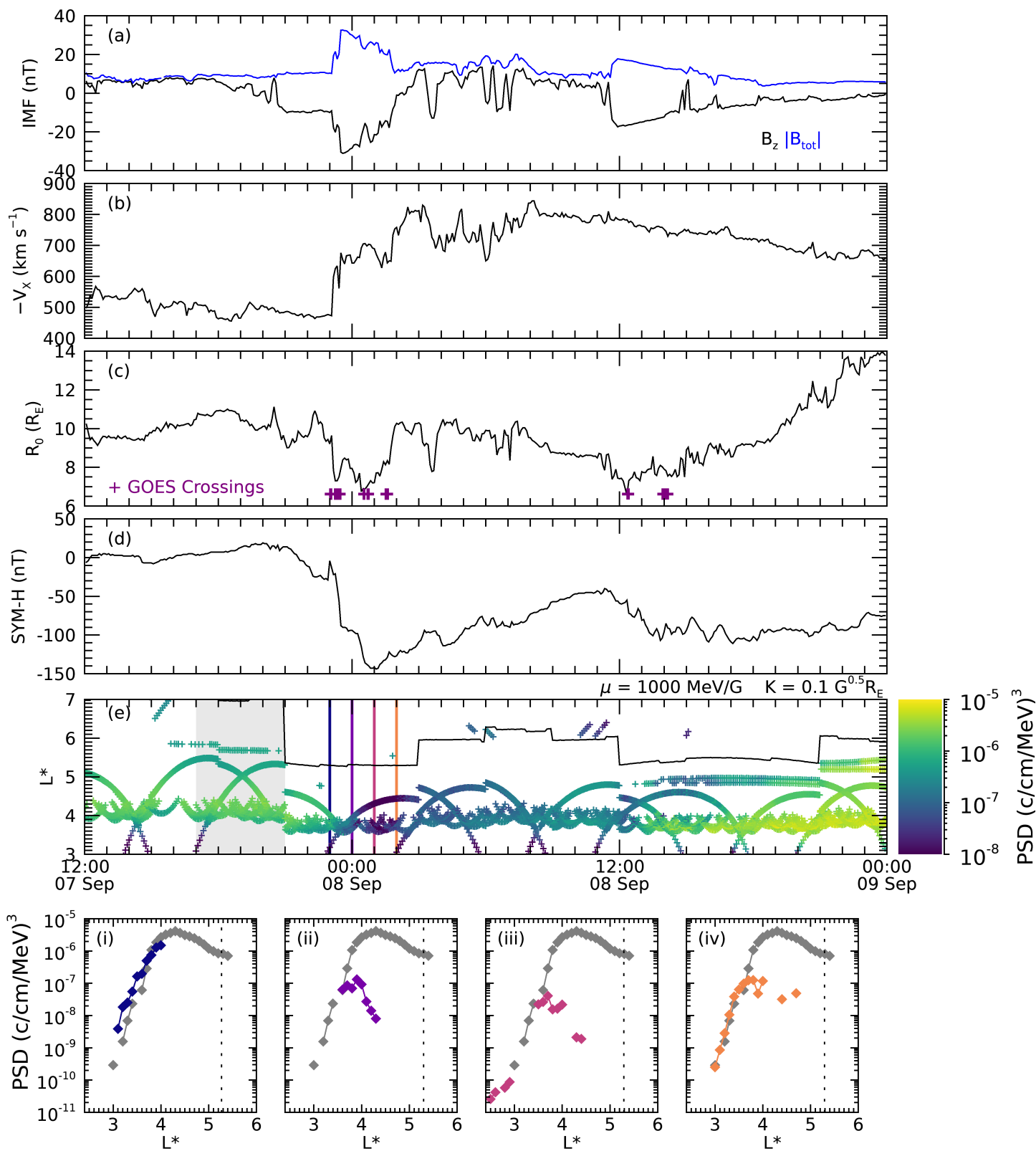
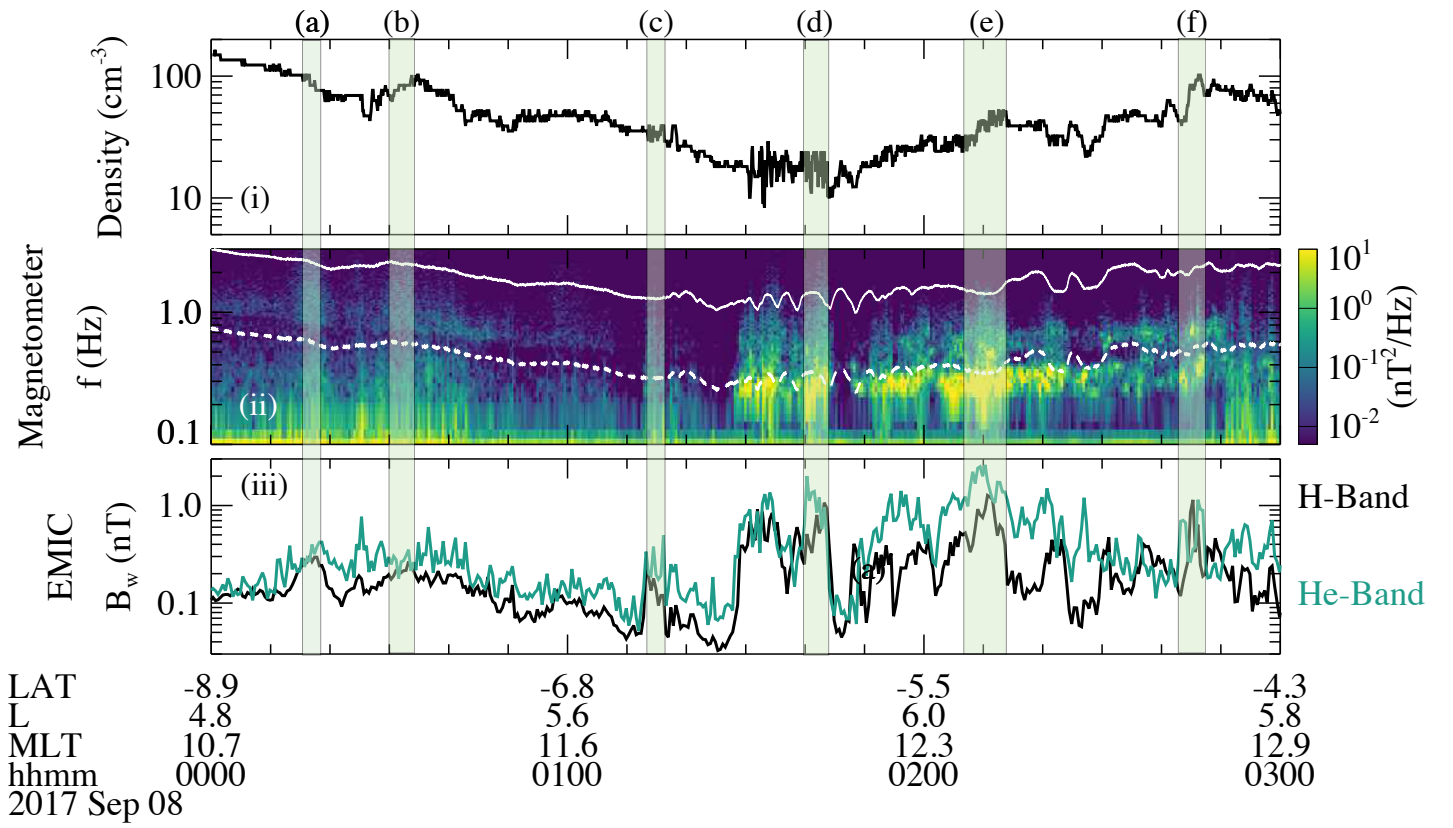


Figure 2.

Van Allen Probe B



$\langle D_{\alpha\alpha} \rangle$ by EMIC + Hiss

H:He:O = 70%:20%:10%

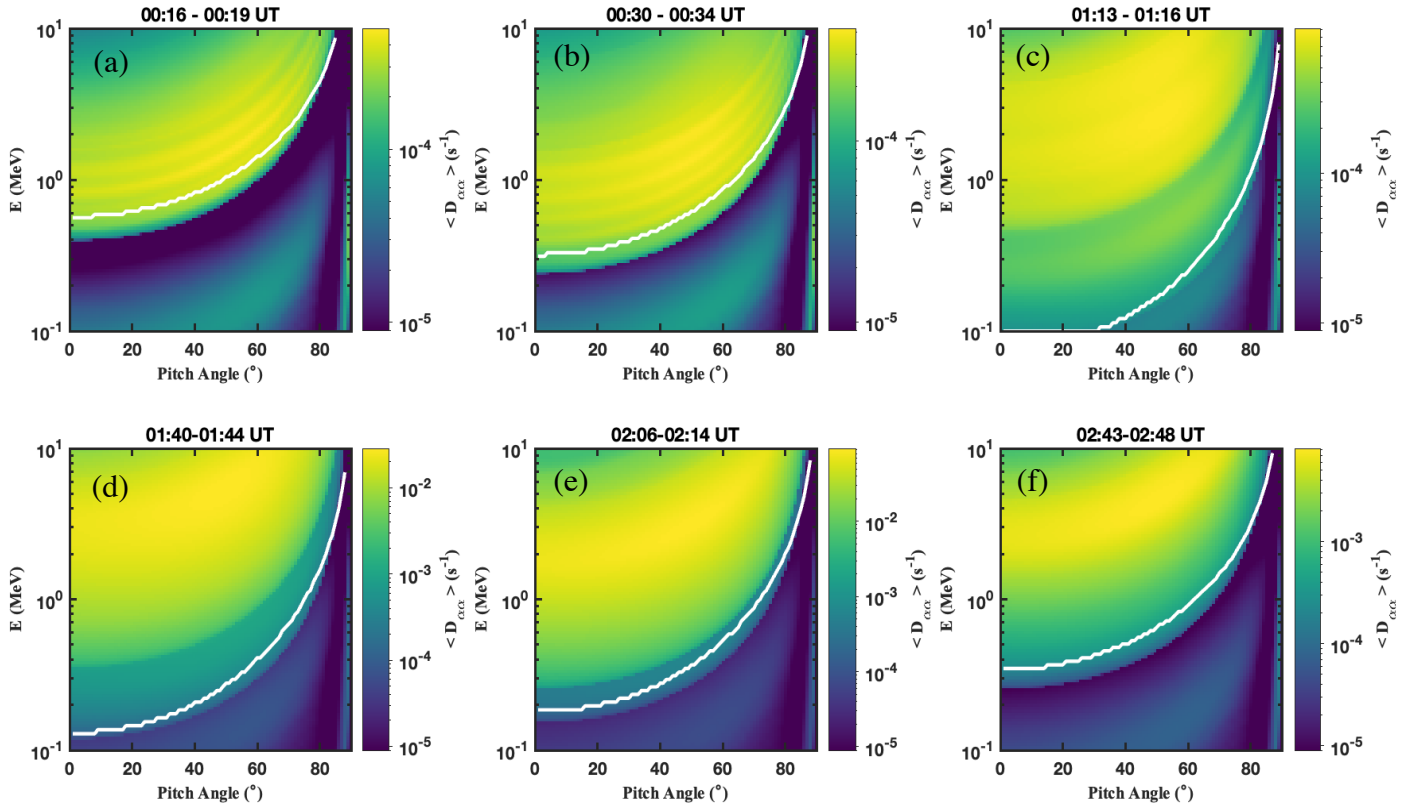


Figure 3.

2D Diffusion Simulation

VAP-B Observations

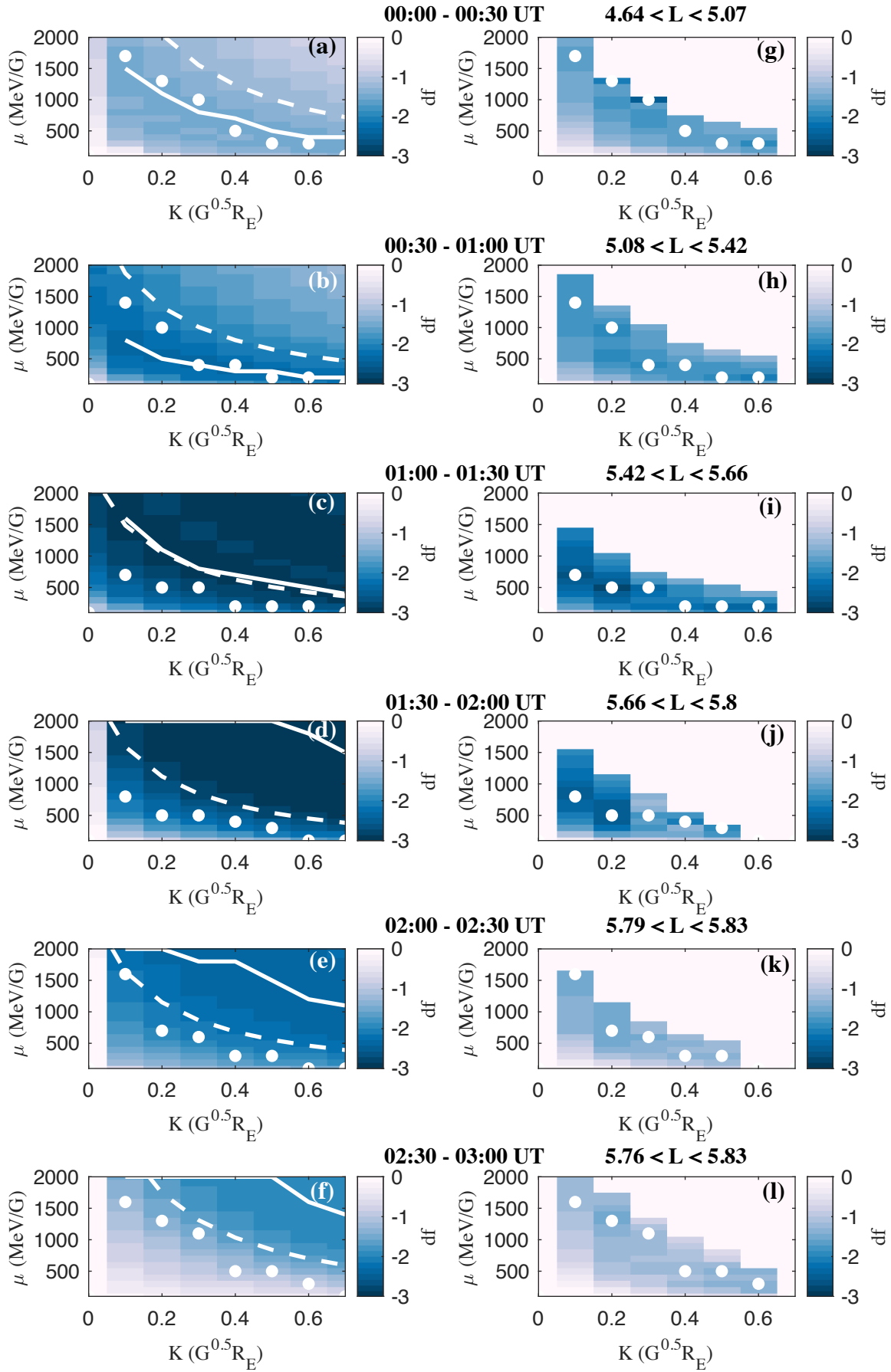
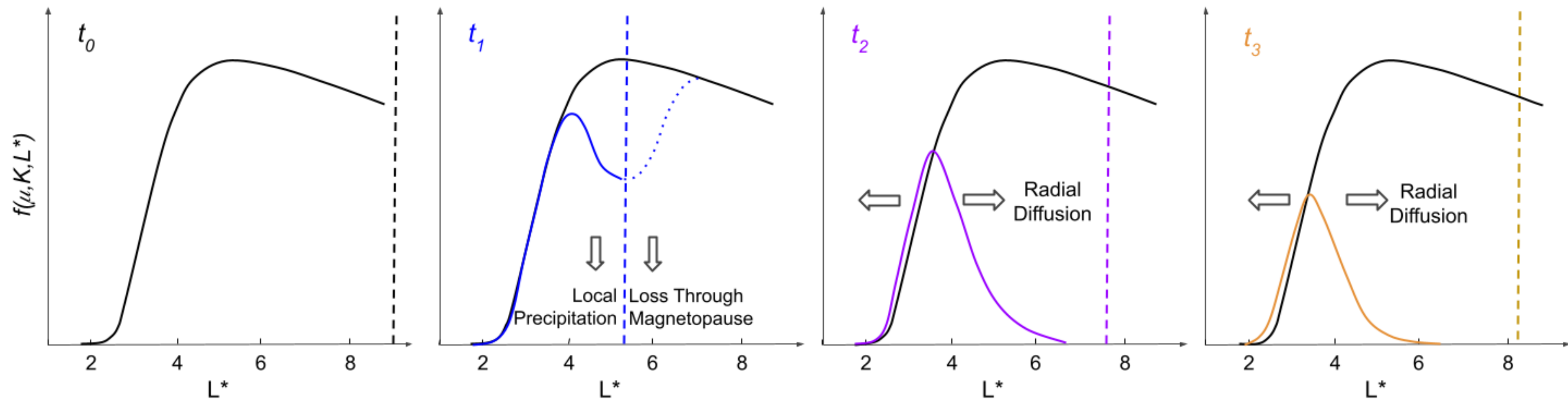


Figure 4.



Differentiating Between Simultaneous Loss Drivers in Earth's Outer Radiation Belt: Multi-Dimensional Phase Space Density Analysis

F. A. Staples¹, Q. Ma^{1,2}, A. Kellerman¹, I. J. Rae³, C. Forsyth⁴, J. K. Sandhu³, J. Bortnik¹

¹Department of Atmospheric and Oceanic Sciences, University of California, Los Angeles, Los Angeles, CA, USA.

²Center for Space Physics, Boston University, Boston, MA, USA.

³Department of Mathematics, Physics and Electrical Engineering, Northumbria University, Newcastle upon Tyne, UK.

⁴Mullard Space Science Laboratory, University College London, London, UK.

Corresponding Author: Frances Staples (fastaples@atmos.ucla.edu)

Key points

- Characterizing electron loss through peaks and minima in radial phase space density can misrepresent simultaneous loss mechanisms.
- Analysis of electron loss across all adiabatic invariants μ , K , and L^* , is necessary to correctly identify loss mechanisms.
- Observational analysis of phase space density data alone cannot be used to quantify individual contributions of simultaneous loss processes.

Abstract

We analyzed the contribution of electromagnetic ion cyclotron (EMIC) wave driven electron loss to a flux dropout event in September 2017. The evolution of electron phase space density (PSD) through the dropout showed the formation of a radially peaked PSD profile as electrons were lost at high L^* , resembling distributions created by magnetopause shadowing. By comparing 2D Fokker Planck simulations of pitch angle diffusion to the observed change in PSD, we found that the μ and K of electron loss aligned with maximum scattering rates at dropout onset. We conclude that, during this dropout event, EMIC waves produced substantial electron loss. Because pitch angle diffusion occurred on closed drift paths near the last closed drift shell, no radial PSD minimum was observed. Therefore, the radial PSD gradients resembled solely magnetopause shadowing loss, even though the local pitch angle scattering produced electron losses of several orders of magnitude of the PSD.

Plain Language Summary

Extremely energetic charged particles become trapped by Earth's geomagnetic field, forming the Van Allen radiation belts. The total amount of radiation trapped within these belts varies depending on the solar wind conditions, which can disturb the geomagnetic field to produce geomagnetic storms. At the beginning of a geomagnetic storm, there is a relative calm in the radiation belt, produced by the rapid drainage of electrons from the geomagnetic field. It is not fully understood if these electrons are primarily lost into the solar wind, or if they are lost into Earth's atmosphere. In this study, we analyze the remaining trapped electrons to reconstruct the mechanisms of electron escape at the beginning of a geomagnetic storm in September 2017. While previous work found that electrons were primarily lost into the solar wind, we found that loss into the atmosphere also played an important role. Furthermore, we showed that drainage of electrons into the atmosphere can be mistaken for loss into the solar wind if the energy and trajectory of lost electrons are not carefully considered.

1 Introduction

Relativistic electron flux in the outer radiation belt is highly variable, changing on timescales from seconds to years (e.g., Abel & Thorne, 1998; Mann & Ozeke, 2016; Nakamura et al., 2000). These changes are controlled by a variety of acceleration and loss mechanisms acting independently or in tandem (Friedel et al., 2002; Reeves et al., 2003; Ripoll et al., 2020). One of the fastest and most dramatic changes to electron flux is radiation belt flux dropouts, when trapped electron populations are observed to suddenly decrease by a factor of 50 or more at a wide range of L-shells, energies, and pitch angles (Pierrard et al., 2020; Turner et al., 2012a; Turner & Ukhorskiy, 2020; Xiang et al., 2018). Losses are either produced by wave-particle interactions which scatter electrons into the atmospheric loss cone (Horne & Thorne, 1998; Kennel & Petschek, 1966; Miyoshi et al., 2008; Thorne & Kennel, 1971), or through the magnetopause into interplanetary space, termed ‘magnetopause shadowing’ (Green et al., 2004; X. Li et al., 1997; Morley et al., 2010; Shprits et al., 2006). The extent to which magnetopause shadowing and atmospheric precipitation each contribute to a radiation belt dropout has been a topic of continuing debate (e.g., Bortnik et al., 2006; Morley et al., 2010; Shprits et al., 2017; Staples et al., 2022; Turner et al., 2014; Turner et al., 2012b; Xiang et al., 2017; Zhang et al., 2016).

A useful tool to distinguish loss mechanisms is phase space density (PSD) analysis of electron dynamics in adiabatic invariant coordinates (μ , K , L^*), which reveal non-adiabatic changes to electron populations (e.g., Degeling et al., 2008; Green & Kivelson, 2004; Selesnick & Blake, 2000). Magnetopause shadowing is typically characterized by PSD loss outside of the last closed drift shell (LCDS), where electron drift paths intersect the magnetopause, followed by diffusive transport across radial gradients in L^* towards the magnetopause (Loto'aniu et al., 2010; Shprits et al., 2006; Turner et al., 2012b). This process creates a localized peak in radial PSD profiles during flux dropouts (illustrated by Turner et al., 2012b). Precipitation to the atmosphere is characterized by PSD loss at a localized L^* , which may create a minimum in radial PSD profiles (Aseev et al., 2017; Blum et al., 2020; Capannolo et al., 2018; Shprits et al., 2018; Shprits et al., 2017). A local minimum in PSD must be observed to deepen over time to interpret with certainty that precipitation produces PSD loss, rather than magnetopause shadowing followed by inward radial

diffusion. Hence, satellite observations over multiple orbits are usually required to attribute loss observations to localized precipitation. Xiang et al. (2017) discussed how observations of PSD at a wide range of μ and K , for a given L^* , provide credible clues to the dominant mechanism of electron loss. For example, EMIC wave scattering of electrons into the loss cone results in depletions at μ and K values associated with electron energies resonant with EMIC waves (Drozdov et al., 2022; X. Ma et al., 2020; Xiang et al., 2018).

In this work we investigated the dependence of PSD loss over a wide range of μ and K during an electron flux dropout which took place in September 2017, following an extreme magnetospheric compression. Staples et al. (2022) previously identified that magnetopause shadowing was the dominant mechanism of electron loss during this dropout, based upon the evolution of PSD characteristics as a function of L^* . However, such extreme magnetospheric compressions are also known drivers of EMIC wave generation (Anderson & Hamilton, 1993; Engebretson et al., 2002; Usanova et al., 2008; Xue et al., 2021). This paper aims to understand if localized precipitation into the atmosphere was appreciable during the dropout by analyzing PSD loss at a wide range of μ and K values.

2 Data and Methodology

2.1 Phase Space Density Dataset

PSD observations between 7 – 9 September 2017 were taken from 32 individual satellites which are part of 5 different scientific missions and hosted payloads. This dataset achieves the highest temporal and spatial resolution of existing combined PSD observations of the radiation belt:

- Van Allen Probe Magnetic Electron Ion Spectrometer (MagEIS) and Relativistic Electron-Proton Telescope (REPT) instruments (Baker et al., 2014; Blake et al., 2014). 2 probes.
- GOES 13, 15 (Geostationary Operational Environmental Satellite) Magnetospheric Electron Detector (MAGED) Energetic Proton, Electron, and Alpha Detector (EPEAD) (Rodriguez, 2014a, 2014b; Sillanpää et al., 2017). 2 probes.
- GPS (Global Positioning System) Navstar Combined X-ray Dosimeter (CXD) (Tuszewski et al., 2004). 21 probes.

- THEMIS (Time History of Events and Macroscale Interactions during Substorms) Electrostatic Analyzer (ESA) and Solid State Telescope (SST) (Angelopoulos, 2008; Angelopoulos et al., 2008; McFadden et al., 2008). 3 Probes.
- MMS (Magnetospheric Multiscale) Fly's Eye Electron Proton Spectrometer (FEEPS) (Blake et al., 2016; Burch et al., 2016). 4 probes.

Intercalibrations between satellites were completed following Staples et al. (2022). All spacecraft data is calibrated to Van Allen Probe B and bias corrected GOES 15 data, which are chosen as "gold standard". In this work GPS pitch angle distributions were assumed using the Zhao et al. (2018) model. For each spacecraft instrument, the adiabatic invariants μ , K , and L^* were computed using either a realistic magnetospheric field model, represented by the International Geomagnetic Reference Field model (IGRF; Thébault et al., 2015) and Tsyganenko (1989) external magnetic field model (T89), or a dipolar field configuration.

2.2 2D Fokker Planck Diffusion Simulation

We used the Full Diffusion Code at University of California, Los Angeles, to calculate the electron diffusion coefficients due to EMIC waves (Q. Ma et al., 2019). The magnetic power spectra of EMIC waves were measured by the Electric and Magnetic Field Instrument Suite and Integrated Science (EMFISIS; Kletzing et al., 2013) instrument on Van Allen Probe B. Diffusion coefficients were calculated for six separate EMIC wave observations, each selected based upon EMIC wave power spectrogram over 30-minute windows through the dropout interval, 00 – 03 UT on 8 September 2017 (see Figure 2), summarized in Supplementary Table S1. The EMIC wave normal angle distribution was assumed to change from quasi-field aligned at the equator to more oblique at higher latitudes, according to the latitudinally-varying model in Ni et al. (2015). The latitude of the wave power was assumed to span from the equator to 40°, and below the latitude where the wave frequency equals the crossover frequency. We considered 3 ion species with composition ratios of 70% H⁺, 20% He⁺ and 10% O⁺ (Meredith et al., 2003), and multiple harmonic resonances (up to 5 orders) and Landau resonance between electrons and EMIC waves. Electron scattering by hiss waves was incorporated into diffusion coefficients by using the statistical hiss wave frequency

spectrum (W. Li et al., 2015). The diffusion coefficients due to hiss waves were much smaller than those due to EMIC waves at energies above 1 MeV, except for the high pitch angles close to 90°. After the bounce-averaged diffusion coefficients were computed, we performed 2D Fokker Planck simulations of the electron PSD evolution due to the resonant interaction with EMIC waves. The 2D Fokker Planck equation was numerically solved using the Alternative Direction Implicit method (Q. Ma et al., 2012). The initial conditions and boundary conditions used in the simulation are detailed in Supplementary Text S1. The simulation was performed for 4-hours using the observed EMIC wave amplitudes. The electron PSD at each energy decreased exponentially with time shortly after the simulation starts. The time scale of the exponential decay corresponds to the electron lifetime, which is energy dependent. The simulated electron PSD evolution was not directly compared with observed dropouts because the MLT coverage of EMIC waves is uncertain. As will be shown in the following analysis, we compared the simulated μ and K dependences of electron PSD decay with the observation, after transforming the pitch angle and energy dependence into the adiabatic invariant coordinates for a dipolar magnetic field.

3 Event Analysis

The compound geomagnetic storm between 7-9 September 2017 was driven by a sequence of interacting coronal mass ejecta (CME) and interplanetary shocks travelling through the solar wind (Scolini et al., 2020; Shen et al., 2018; Werner et al., 2019). Figure 1 summarizes the radiation belt response to the solar wind and the subsequent geomagnetic conditions. At 23 UT on 7 September, an interplanetary shock arrived at the magnetosphere, indicated by the sudden increase in IMF field strength to 33 nT with a decrease of the B_z component to -31 nT (Figure 1a), and solar wind speed increases to 830 km s⁻¹ (Figure 1b). As a result, the magnetopause was compressed within geostationary orbit (purple crosses, Figure 1c) and the Sym-H index suddenly decreased to -142 nT, indicating storm onset followed by the main phase. Through the main phase of the storm (23 UT 7 September – 01 UT 8 September), electron PSD decreased suddenly by up to 3 orders of magnitude (for $\mu = 1000$ MeV/G and $K = 0.1$ G^{0.5}R_E, Figure 1e). Through the recovery phase of the storm the PSD remained low compared to pre-storm PSD, until 12 UT on 8 September when PSD increased substantially through localized electron acceleration (Staples et al., 2022).

Figure 1i-iv show radial PSD profiles during the dropout between 23 UT on 7 September – 03 UT on 8 September for $\mu = 1000$ MeV/G and $K = 0.1 \text{ G}^{0.5} \text{R}_E$. Each panel compares the hourly averaged PSD to the average pre-storm PSD between 17 - 21 UT on 7 September (gray profiles). Immediately prior to the dropout, between 23 – 24 UT on 7 September, the PSD at $L^* < 4$ was, on average, slightly greater than the pre-storm PSD. At the onset of the dropout during the following hour (Figure 1ii), PSD measurements at $L^* > 3.7$ were up to 3 orders of magnitude less than pre-storm PSD, with greater losses at higher L^* . Between 01 - 02 UT on 8 September (Figure 1iii) loss continued to occur at $L^* > 3.7$; the maximum PSD loss was measured to be over 3 orders of magnitude compared to pre-storm PSD at $L^* = 4.4$. The final interval 02 - 03 UT on 8 September (Figure 1iv) showed the PSD was approximately the same as the pre-storm PSD at $L^* < 3.6$, whereas PSD had decreased by over 2 orders of magnitude compared the pre-storm PSD at $L^* > 3.6$, with greatest loss occurring at high $L^* = 4.4$. PSD at $L^* > 4$ increased substantially between 02 - 03 UT on 8 September (interval iv) compared to the previous hour (interval iii).

Figure 1i-iv shows the formation of a radial PSD peak at $L^* \sim 3.7$ following an incursion of the LCDS, with greatest electron losses observed at $L^* > 3.7$. These characteristics appear consistent with electron loss to the compressed magnetopause, and outward radial diffusion, as concluded by Staples et al. (2022).

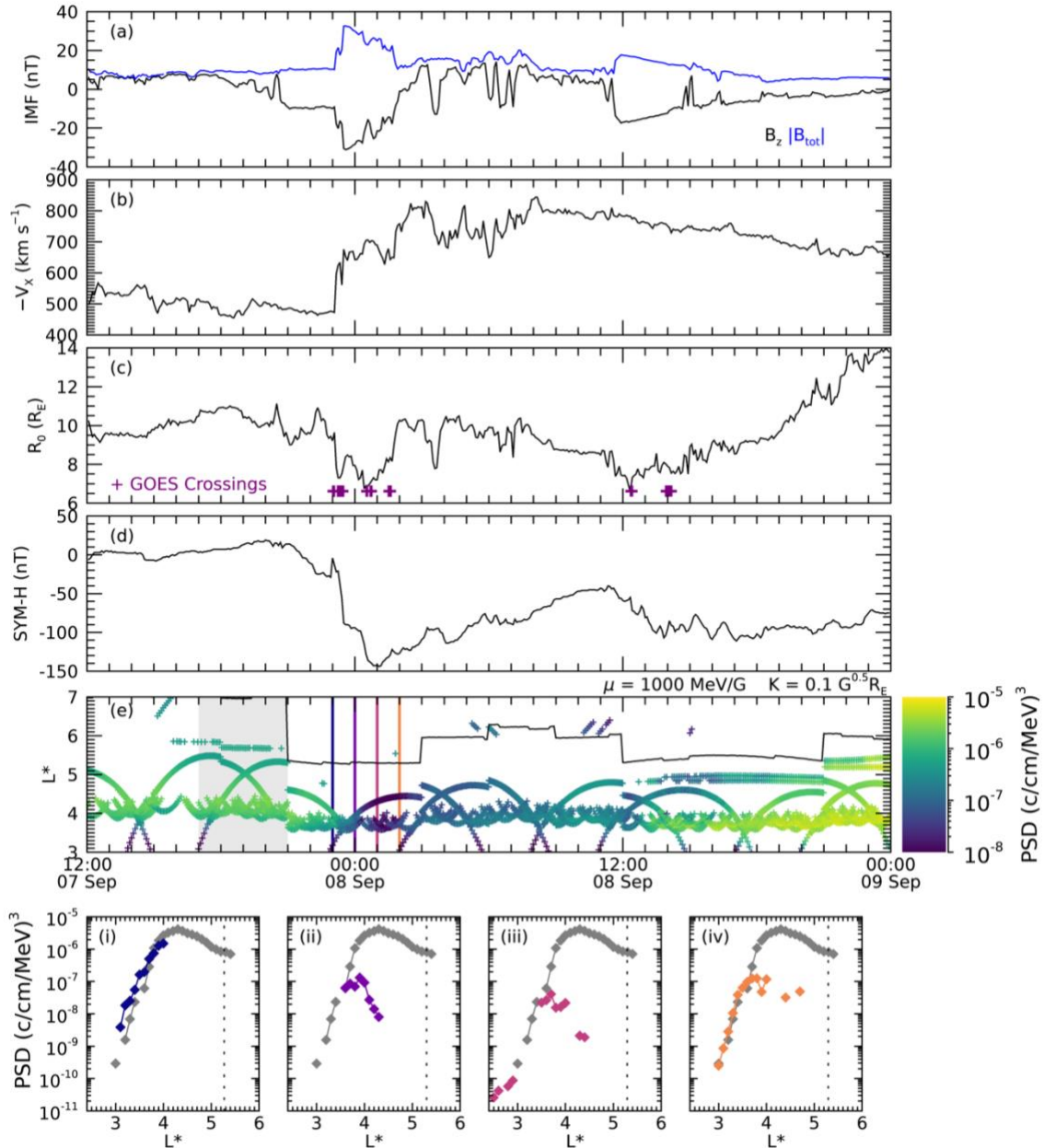


Figure 1 Panels a-e summarize the solar wind, geomagnetic, and radiation belt conditions between 12 UT 7 September – 00 UT 9 September 2017: (a) interplanetary magnetic field strength (blue) and B_z component (black); (b) solar wind speed; (c) subsolar magnetopause (black line, Shue et al., 1998) and radial distance to GOES magnetopause crossings (purple crosses); (d) Sym-H index; (e) PSD of electrons at $\mu = 1000 \text{ MeV/G}$ and $K = 0.1 \text{ G}^{0.5} R_E$. Panels (i-iv) show radial PSD profiles. The grey profile on all panels references the average pre-storm PSD, the colored profiles show hourly PSD through the dropout, the beginning time of each hour is indicated by correspondingly colored vertical lines in panel (e). The location of the LCDS is indicated by the black line in panel (e) and vertical dashed lines in panels (i-iv).

To analyze whether localized precipitation to the atmosphere contributed to electron loss during the dropout, we searched for EMIC wave signatures using EMFISIS observations of the magnetic power spectra. Strong EMIC waves were identified during the flux dropout, between 00 - 03 UT on 8 September, observed by Van Allen Probe B on an outbound orbit towards apogee at noon, summarized in Figure 2. Figure 2i shows that the total electron density was between $10 - 100 \text{ cm}^{-3}$, and significant power spectral density was observed below the equatorial H^+ and He^+ gyrofrequencies (Figure 2ii), indicating the presence of H^+ band and He^+ band EMIC waves. The integrated wave amplitude of the H^+ and He^+ frequency wave bands (Figure 2iii) show that He^+ band waves were higher in amplitude throughout the interval, with the largest amplitude waves observed between 01:300 – 02:30 UT 8 September, reaching a maximum amplitude of $> 2 \text{ nT}$ in the He^+ band and $> 1 \text{ nT}$ in the H^+ band.

Figure 2a-f show bounce averaged electron pitch angle diffusion coefficients, $D_{\alpha\alpha}$, computed using the averaged EMIC wave spectra of the observed wave bursts (labelled on panels i-iii) and statistical hiss wave spectra. Figure 2a-f show that EMIC waves could interact with electrons at very low energies in the $\sim 100\text{s}$ of keV range for equatorial electrons with pitch angles $< 70^\circ$ and $\sim \text{MeV}$ range for electrons with equatorial pitch angles $> 70^\circ$. The high EMIC wave power in the He^+ band between 01:30 – 02:30 UT resulted in extremely high pitch angle diffusion coefficients of $> 0.001 \text{ s}^{-1}$ for electron energies $> 400 \text{ keV}$ and pitch angles $< 70^\circ$. While diffusion timescales of electrons varied greatly upon energy and pitch angles, Figure 2 nonetheless demonstrates that EMIC wave-particle interactions could produce rapid diffusion of electrons towards the loss cone during the dropout.

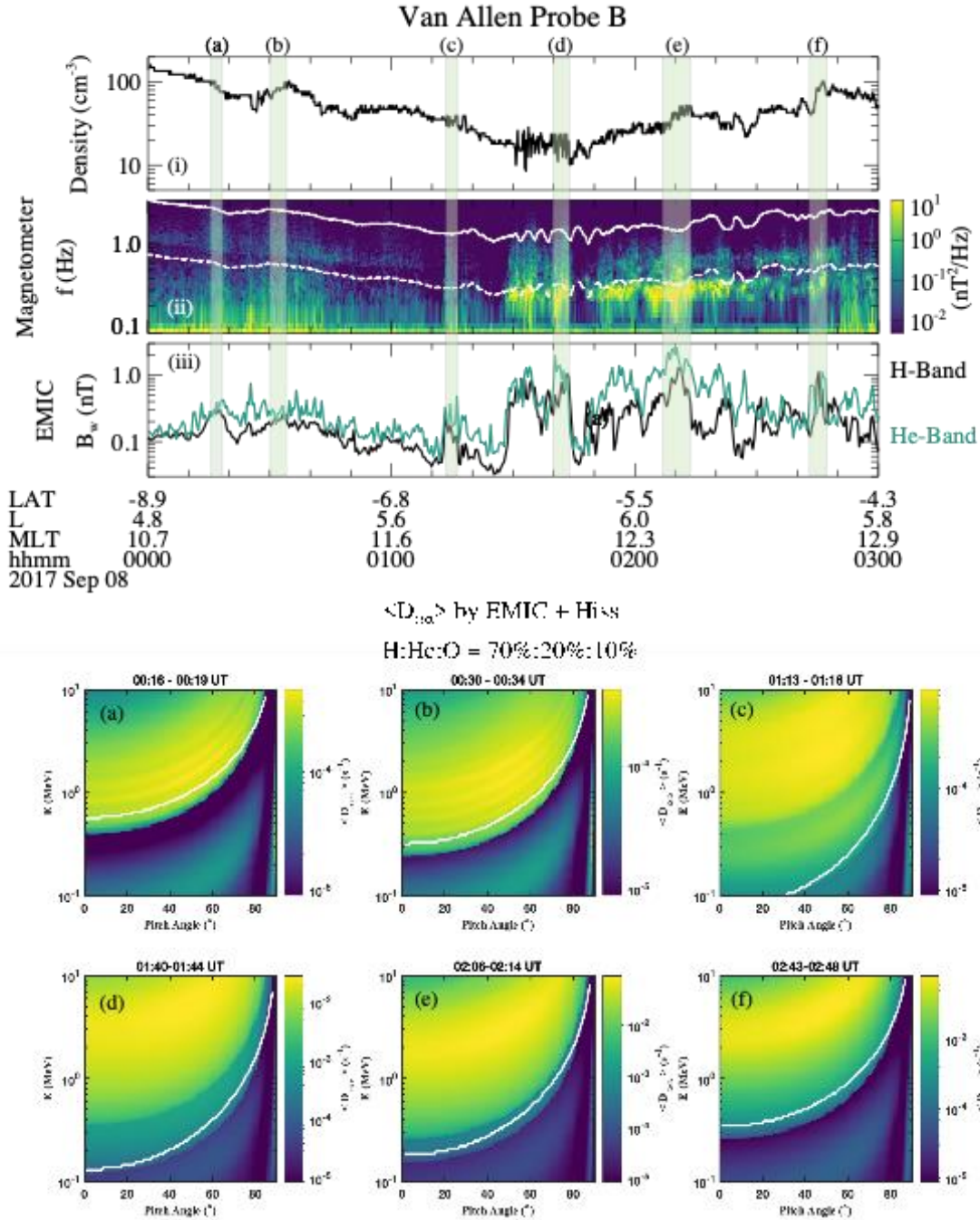


Figure 2. Van Allen Probe B observation of EMIC waves and the bounce-averaged diffusion coefficients. (i) Total electron density; (ii) magnetic wave power spectrogram, where the white solid and dashed lines are equatorial ion gyrofrequencies f_{cp} and f_{He} , respectively; (iii) H^+ band and He^+ band EMIC wave amplitudes. Green shaded boxes over i-iii indicate the times of EMIC wave samples a-f. Pitch angle diffusion coefficients, $D_{\alpha\alpha}$, computed from statistical hiss and sampled EMIC waves are displayed as a function of energy and pitch angle in panels a-f. White lines in panels a-f indicate minimum resonant energies between electrons and EMIC waves.

Figure 3 compares the simulated change in electron PSD during the dropout (Figure 3a-f, left column) to the observed change in PSD (Figure 3g-l, right column) as a function of μ and K . Each row shows the simulated and observed df for the case of each 30-minute window during the dropout period, where df is described by Equation 1. Because simulations of df were conducted in a dipolar magnetic field, PSD observations presented in Figure 3 were also converted into adiabatic coordinates using a dipolar magnetic field to allow for comparison.

$$df = \log_{10} \left(\frac{\text{Dropout PSD}}{\text{Pre-storm PSD}} \right) \quad \text{Equation 1}$$

For the case of both simulated and observed df , 'Pre-storm PSD' was set to average Van Allen Probe B observation between 17 – 21 UT on 7 September (gray shaded area Figure 1e). For simulated df , the 'Dropout PSD' for each 30-minute window was determined by a 2D Fokker-Plank simulation of electron diffusion which used diffusion coefficients calculated from sampled EMIC wave spectra (see Figure 2) and statistical hiss wave spectra (described in Section 2.2). The initial condition of this simulation was equal to the 'Pre-storm PSD'. The final simulated PSD values were determined when the 2 MeV electron PSD matched the average PSD sampled by Van Allen Probe B during the 30-minute window. For the case of observed df , 'Dropout PSD' was the PSD averaged over 30-minute windows between 00 - 03 UT on 8 September (between purple-orange lines Figure 1e). Note that the observed L range overlapped between windows because a wide sample of electron pitch angles is considered as the probe follows an outbound orbit.

Figure 3 shows that PSD decreased ($df < 0$) compared to the pre-storm interval at nearly all μ and K values across the phase space, and PSD decrease exemplified pitch angle scattering loss instead of magnetopause shadowing effects: Throughout the dropout the magnitude of PSD loss was observed to be highly dependent on μ and K , with maximum PSD loss (white dots) showed a non-linear relationship between μ and K , corresponding to the energy and pitch angle dependent loss mechanism. At the onset of the dropout, between 00 – 01 UT (Figure 3a,b), the μ and K values of maximum observed PSD loss aligned with the maximum simulated PSD loss for EMIC wave

scattering. This serves as compelling evidence that PSD loss was produced by EMIC wave scattering between $4.46 < L < 5.42$.

Observations between 01 - 02 UT showed the greatest PSD decrease through the orbit of Van Allen Probe B (Figure 3i-j), with $df < 3$ for $\mu \sim 600$ MeV/G and $K \sim 0.2 \text{ G}^{0.5} \text{R}_E$. While the maximum PSD loss after 01 UT followed a similar relationship between μ and K as earlier in the dropout, the maximum observed df did not coincide with simulated df through EMIC wave scattering. The simulated df estimated that maximum PSD loss would occur at very high μ (multi-MeV), corresponding to energy channels where electron flux was measured at the instrument noise floor (above dashed white line). Nonetheless, simulated PSD loss showed that EMIC waves were capable of scattering electrons at μ and K below the noise floor by similar orders of magnitude as Van Allen Probe B observations. There could be several reasons why the maximum observed PSD loss after 01 UT did not align in μ and K with the maximum simulated PSD loss, such as inaccuracies in the assumptions made when calculating simulation diffusion coefficients. For example, the EMIC waves with a different frequency spectrum from that observed by Van Allen Probe B in Figure 2ii could occur at other MLT sectors or times which were not sampled by the satellite. Furthermore, an assumed ion composition ratio was used, which could alter the energy and pitch angle dependence of pitch angle diffusion (Kang et al., 2015).

Observations between 02 - 03 UT (Figure 3k-l) show that $|df|$ was smaller than the previous hour (Figure 3i-j) at all μ and K . This shows that acceleration processes acted to produce a net-increase in PSD after ~ 02 UT compared to the previous hour, which is supported by high resolution multi-mission PSD observations presented in Figure 1iii-iv. Because acceleration also produced changes to observed df during this hour, we cannot differentiate the effects of EMIC wave scattering across all μ and K .

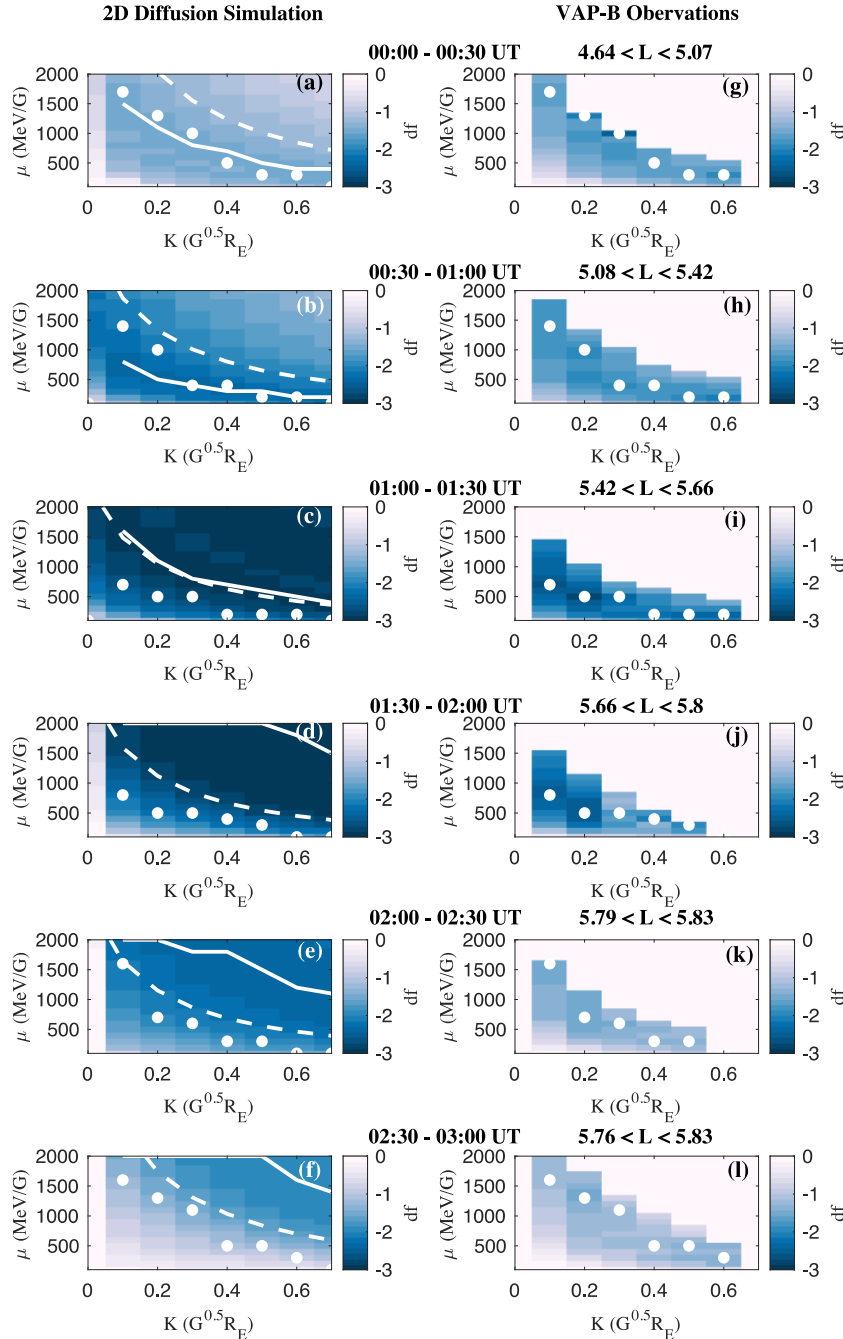


Figure 3 Left Column (a-f) shows simulated change in PSD, df , based upon EMIC wave observations sampled over 30-minute windows during the PSD dropout between 00 UT 8 September – 03 UT 8 September. Right column (g-l) shows corresponding Van Allen Probe B observations of average PSD change, df , over each window. Observed and simulated df are shown by color as a function of μ and K , approximated in a dipolar magnetic field. Solid white lines/dots show the values of maximum simulated/observed PSD loss (minimum df) as a function of μ . The dashed white line indicates the maximum measurable μ after taking the noise floor into consideration.

4 Conclusion

This study examined the characteristics of electron loss induced by EMIC wave-particle interactions by considering changes to electron PSD as a function of the first and second adiabatic invariants. In the event analyzed in September 2017, an electron flux dropout was produced following a strong magnetospheric compression and geomagnetic storm. Previous work identified magnetopause shadowing as the dominant loss mechanism through analysis of radial PSD profiles across L^* (Staples et al., 2022). In our analysis, we also found that the evolution of radial PSD profiles through the dropout interval showed characteristics of magnetopause shadowing; a radial PSD peak was formed following an incursion of the LCDS, and no PSD minima were observed to deepen over time (Figure 1i-iv). However, observations from Van Allen Probe B showed significant wave power in both H^+ and He^+ EMIC wave bands between 0 – 3 UT on 8 September. Simultaneously, Van Allen Probe B observed concurrent electron PSD loss by up to 3 orders of magnitude compared to the pre-storm interval (Figure 3). We found that observed PSD loss was closely reproduced by a 2D Fokker-Plank simulation which modelled diffusion by sampled EMIC wave observations, and statistical hiss waves, at the onset of the dropout 00 -01 UT 8 September (Figure 3a-b,g-h). PSD loss observed during the latter part of the dropout was found to be more difficult to analyze through simulation because the electron fluxes were reduced to the instrument noise floor, limiting PSD observations at high energies. Nonetheless, the observations of PSD loss at dropout onset provided compelling evidence that EMIC wave driven electron scattering contributed to electron loss for electrons at $L^* > 4$.

We argue that during this flux dropout event, EMIC wave-particle interactions produced electron loss on closed drift paths, whereas magnetopause shadowing produced electron loss on open drift paths beyond the LCDS. Figure 4 provides an illustration of PSD evolution for this scenario: At time t_0 the PSD profile represents a pre-storm distribution which is radially peaked at $L^* = 5$. Time t_1 represents a period of strong magnetospheric compression which causes the LCDS to decrease to low L^* , and EMIC waves are generated in the outer magnetosphere, near the LCDS. As a result, electrons on open drift paths beyond the LCDS are lost across the magnetopause, and on closed drift paths EMIC waves drive rapid pitch angle diffusion and subsequent loss to the

atmosphere. The location of the LCDS relative to EMIC wave activity obscures any radial PSD minimum created by local precipitation. Time t_2 represents a relaxation of the magnetosphere, and the LCDS increases to higher L^* . Combined losses to the magnetopause and atmosphere at high L^* result in a localized peak in PSD and steep radial PSD gradients. Time t_3 represents how ULF wave driven radial diffusion could act to smooth radial gradients produced by losses. This scenario demonstrates that simultaneous loss processes at high L^* result in a PSD evolution which was previously interpreted as magnetopause loss only. Only when analyzing PSD loss as a function of μ and K do EMIC wave-particle interaction characteristics come to light.

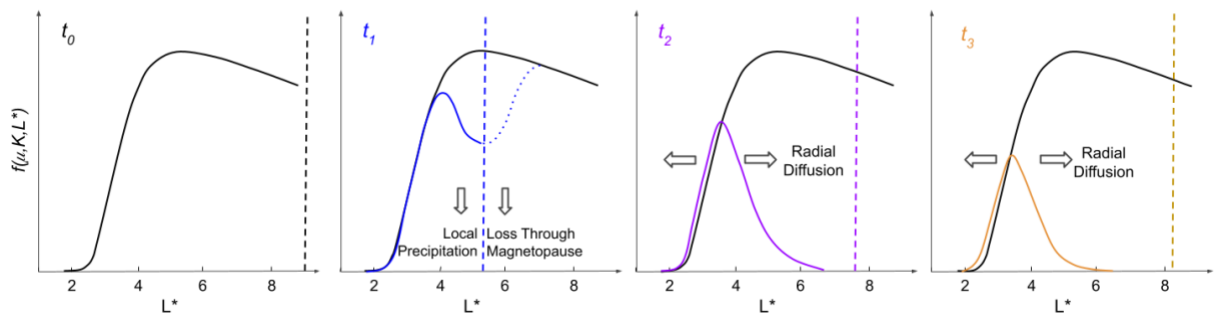


Figure 4 Diagram of PSD evolution over four time periods $t_0 - t_3$ (left to right) as a function of L^* for a scenario where magnetopause shadowing produces electron loss on open drift paths, and EMIC wave-particle interactions produce fast precipitation to the atmosphere inside of the LCDS. Vertical dashed lines represent the LCDS. The blue dotted line in panel t_1 illustrates PSD profile if local precipitation acted alone to produce a localized PSD loss.

It is an unexpected finding that local wave-particle interactions could be an effective loss mechanism near the LCDS for two reasons: First, EMIC wave interactions typically produce scattering of \sim MeV electrons (Usanova et al., 2014), but the observed loss was across a wide range of radiation belt energies > 100 s keV. Second, efficient electron scattering by EMIC waves usually occurs in the overlapped region of the ring current and the high-density plasmasphere, where the minimum resonance energy is reduced (Meredith et al., 2003; Summers et al., 2007). In the September 2017, the drainage of electrons into the outer magnetosphere during the main phase of the geomagnetic storm (Figure 2i) provided higher than usual plasma density in the outer magnetosphere, allowing EMIC waves to interact with lower energy electrons (100s of keV). In addition, the magnetosphere was extremely compressed (Figure 1c), so the LCDS was located at

323 low L^* relative to localized EMIC wave-particle interactions. This is an important finding because
324 the conclusion is contrary to the previous understanding that a negative gradient in PSD towards
325 the LCDS is indicative of magnetopause shadowing loss.

Acknowledgements

We acknowledge the developers of the IRBEM library, which was used to compute adiabatic invariant coordinates (Boscher et al., 2013). The computations employed computational and storage services associated with the Hoffman2 Shared Cluster provided by UCLA Institute for Digital Research and Education's Research Technology Group. ACK acknowledges high-performance computing support from Cheyenne (<https://doi.org/10.5065/D6RX99HX>) provided by NCAR's Computational and Information Systems Laboratory, sponsored by the National Science Foundation.

FS was supported by NASA grants 80NSSC20K1402 and NSF grant 2149782. ACK acknowledges support from NASA grants 80NSSC20K1402 and 80NSSC20K1281, and NSF grant 2149782. QM acknowledges the NASA grant 80NSSC20K0196, and NSF grant AGS-2225445. IJR and JKS acknowledge support from NERC grants NE/P017185/2, NE/V002554/2 and STFC grant ST/V006320/1. CF was supported by NERC IRF NE/N014480/1 and NERC grants NE/P017185/1 and NE/V002554/2.

Open Research

Multi-mission phase space density observations presented in this study are publicly available via 10.5281/zenodo.7293955. Spacecraft data from GOES and the Van Allen Probes are publicly available via the NASA/GSFC CDAWeb service (<https://cdaweb.gsfc.nasa.gov/index.html/>). Solar Wind data and geomagnetic indices are publicly available through the NASA/GSFC Space Physics Data Facility OMNIWeb service (<https://omniweb.gsfc.nasa.gov/>).

References

- Abel, B., & Thorne, R. M. (1998). Electron scattering loss in Earth's inner magnetosphere: 1. Dominant physical processes. *Journal of Geophysical Research: Space Physics*, 103(A2), 2385-2396. <https://agupubs.onlinelibrary.wiley.com/doi/abs/10.1029/97JA02919>
- Anderson, B. J., & Hamilton, D. C. (1993). Electromagnetic ion cyclotron waves stimulated by modest magnetospheric compressions. *Journal of Geophysical Research: Space Physics*, 98(A7), 11369-11382. <https://agupubs.onlinelibrary.wiley.com/doi/abs/10.1029/93JA00605>
- Angelopoulos, V. (2008). The THEMIS Mission. *Space Science Reviews*, 141(1), 5. <https://doi.org/10.1007/s11214-008-9336-1>
- Angelopoulos, V., Sibeck, D., Carlson, C. W., McFadden, J. P., Larson, D., Lin, R. P., et al. (2008). First Results from the THEMIS Mission. *Space Science Reviews*, 141(1), 453-476. <https://doi.org/10.1007/s11214-008-9378-4>
- Aseev, N. A., Shprits, Y. Y., Drozdov, A. Y., Kellerman, A. C., Usanova, M. E., Wang, D., & Zhelavskaya, I. S. (2017). Signatures of Ultrarelativistic Electron Loss in the Heart of the Outer Radiation Belt Measured by Van Allen Probes. *Journal of Geophysical Research: Space Physics*, 122(10), 10,102-110,111. <https://agupubs.onlinelibrary.wiley.com/doi/abs/10.1002/2017JA024485>
- Baker, D. N., Kanekal, S. G., Hoxie, V. C., Batiste, S., Bolton, M., Li, X., et al. (2014). The Relativistic Electron-Proton Telescope (REPT) Instrument on Board the Radiation Belt Storm Probes (RBSP) Spacecraft: Characterization of Earth's Radiation Belt High-Energy Particle Populations. In N. Fox & J. L. Burch (Eds.), *The Van Allen Probes Mission* (pp. 337-381). Boston, MA: Springer US.
- Blake, J. B., Carranza, P. A., Claudepierre, S. G., Clemmons, J. H., Crain, W. R., Dotan, Y., et al. (2014). The Magnetic Electron Ion Spectrometer (MagEIS) Instruments Aboard the Radiation Belt Storm Probes (RBSP) Spacecraft. In N. Fox & J. L. Burch (Eds.), *The Van Allen Probes Mission* (pp. 383-421). Boston, MA: Springer US.
- Blake, J. B., Mauk, B. H., Baker, D. N., Carranza, P., Clemmons, J. H., Craft, J., et al. (2016). The Fly's Eye Energetic Particle Spectrometer (FEEPS) Sensors for the Magnetospheric Multiscale (MMS) Mission. *Space Science Reviews*, 199, 309. <https://ui.adsabs.harvard.edu/abs/2016SSRv..199..309B>
- Blum, L. W., Remya, B., Denton, M. H., & Schiller, Q. (2020). Persistent EMIC Wave Activity Across the Nightside Inner Magnetosphere. *Geophysical Research Letters*, 47(6), e2020GL087009. <https://agupubs.onlinelibrary.wiley.com/doi/abs/10.1029/2020GL087009>
- Bortnik, J., Thorne, R. M., O'Brien, T. P., Green, J. C., Strangeway, R. J., Shprits, Y. Y., & Baker, D. N. (2006). Observation of two distinct, rapid loss mechanisms during the 20 November 2003 radiation belt dropout event. *Journal of Geophysical Research: Space Physics*, 111(A12). <https://agupubs.onlinelibrary.wiley.com/doi/abs/10.1029/2006JA011802>

- 384 Boscher, D., Bourdarie, S., O'Brien, T. P., & Guild, T. (2013). The International Radiation Belt
385 Environment Modeling (IRBEM) library.
- 386 Burch, J. L., Moore, T. E., Torbert, R. B., & Giles, B. L. (2016). Magnetospheric Multiscale Overview
387 and Science Objectives. *Space Science Reviews*, 199(1), 5-21.
388 <https://doi.org/10.1007/s11214-015-0164-9>
- 389 Capannolo, L., Li, W., Ma, Q., Zhang, X.-J., Redmon, R. J., Rodriguez, J. V., et al. (2018).
390 Understanding the Driver of Energetic Electron Precipitation Using Coordinated
391 Multisatellite Measurements. *Geophysical Research Letters*, 45(14), 6755-6765.
392 <https://agupubs.onlinelibrary.wiley.com/doi/abs/10.1029/2018GL078604>
- 393 Degeling, A. W., Ozeke, L. G., Rankin, R., Mann, I. R., & Kabin, K. (2008). Drift resonant generation
394 of peaked relativistic electron distributions by Pc 5 ULF waves. *Journal of Geophysical*
395 *Research: Space Physics*, 113(A2).
396 <https://agupubs.onlinelibrary.wiley.com/doi/abs/10.1029/2007JA012411>
- 397 Drozdov, A. Y., Allison, H. J., Shprits, Y. Y., Usanova, M. E., Saikin, A., & Wang, D. (2022). Depletions
398 of Multi-MeV Electrons and Their Association to Minima in Phase Space Density.
399 *Geophysical Research Letters*, 49(8), e2021GL097620.
400 <https://agupubs.onlinelibrary.wiley.com/doi/abs/10.1029/2021GL097620>
- 401 Engebretson, M. J., Peterson, W. K., Posch, J. L., Klatt, M. R., Anderson, B. J., Russell, C. T., et al.
402 (2002). Observations of two types of Pc 1–2 pulsations in the outer dayside
403 magnetosphere. *Journal of Geophysical Research: Space Physics*, 107(A12), SMP 20-21-SMP
404 20-20. <https://agupubs.onlinelibrary.wiley.com/doi/abs/10.1029/2001JA000198>
- 405 Friedel, R. H. W., Reeves, G. D., & Obara, T. (2002). Relativistic electron dynamics in the inner
406 magnetosphere — a review. *Journal of Atmospheric and Solar-Terrestrial Physics*, 64(2),
407 265-282. <https://www.sciencedirect.com/science/article/pii/S1364682601000888>
- 408 Green, J. C., & Kivelson, M. G. (2004). Relativistic electrons in the outer radiation belt:
409 Differentiating between acceleration mechanisms. *Journal of Geophysical Research: Space*
410 *Physics*, 109(A3). <https://agupubs.onlinelibrary.wiley.com/doi/abs/10.1029/2003JA010153>
- 411 Green, J. C., Onsager, T. G., O'Brien, T. P., & Baker, D. N. (2004). Testing loss mechanisms capable
412 of rapidly depleting relativistic electron flux in the Earth's outer radiation belt. *Journal of*
413 *Geophysical Research: Space Physics*, 109(A12).
414 <https://agupubs.onlinelibrary.wiley.com/doi/abs/10.1029/2004JA010579>
- 415 Horne, R. B., & Thorne, R. M. (1998). Potential waves for relativistic electron scattering and
416 stochastic acceleration during magnetic storms. *Geophysical Research Letters*, 25(15),
417 3011-3014. <https://agupubs.onlinelibrary.wiley.com/doi/abs/10.1029/98GL01002>
- 418 Kang, S.-B., Min, K.-W., Fok, M.-C., Hwang, J., & Choi, C.-R. (2015). Estimation of pitch angle
419 diffusion rates and precipitation time scales of electrons due to EMIC waves in a realistic
420 field model. *Journal of Geophysical Research: Space Physics*, 120(10), 8529-8546.
421 <https://agupubs.onlinelibrary.wiley.com/doi/abs/10.1002/2014JA020644>

- Kennel, C. F., & Petschek, H. E. (1966). Limit on stably trapped particle fluxes. *Journal of Geophysical Research* (1896-1977), 71(1), 1-28.
<https://agupubs.onlinelibrary.wiley.com/doi/abs/10.1029/JZ071i001p00001>
- Kletzing, C. A., Kurth, W. S., Acuna, M., MacDowall, R. J., Torbert, R. B., Averkamp, T., et al. (2013). The Electric and Magnetic Field Instrument Suite and Integrated Science (EMFISIS) on RBSP. *Space Science Reviews*, 179(1), 127-181. <https://doi.org/10.1007/s11214-013-9993-6>
- Li, W., Ma, Q., Thorne, R. M., Bortnik, J., Kletzing, C. A., Kurth, W. S., et al. (2015). Statistical properties of plasmaspheric hiss derived from Van Allen Probes data and their effects on radiation belt electron dynamics. *Journal of Geophysical Research: Space Physics*, 120(5), 3393-3405.
<https://agupubs.onlinelibrary.wiley.com/doi/abs/10.1002/2015JA021048>
- Li, X., Baker, D. N., Temerin, M., Cayton, T. E., Reeves, E. G. D., Christensen, R. A., et al. (1997). Multisatellite observations of the outer zone electron variation during the November 3-4, 1993, magnetic storm. *Journal of Geophysical Research: Space Physics*, 102(A7), 14123-14140. <https://agupubs.onlinelibrary.wiley.com/doi/abs/10.1029/97JA01101>
- Loto'aniu, T. M., Singer, H. J., Waters, C. L., Angelopoulos, V., Mann, I. R., Elkington, S. R., & Bonnell, J. W. (2010). Relativistic electron loss due to ultralow frequency waves and enhanced outward radial diffusion. *Journal of Geophysical Research: Space Physics*, 115(A12).
<https://agupubs.onlinelibrary.wiley.com/doi/abs/10.1029/2010JA015755>
- Ma, Q., Li, W., Yue, C., Thorne, R. M., Bortnik, J., Kletzing, C. A., et al. (2019). Ion Heating by Electromagnetic Ion Cyclotron Waves and Magnetosonic Waves in the Earth's Inner Magnetosphere. *Geophysical Research Letters*, 46(12), 6258-6267.
<https://agupubs.onlinelibrary.wiley.com/doi/abs/10.1029/2019GL083513>
- Ma, Q., Ni, B., Tao, X., & Thorne, R. M. (2012). Evolution of the plasma sheet electron pitch angle distribution by whistler-mode chorus waves in non-dipole magnetic fields. *Ann. Geophys.*, 30(4), 751-760. <https://angeo.copernicus.org/articles/30/751/2012/>
- Ma, X., Xiang, Z., Ni, B., Fu, S., Cao, X., Hua, M., et al. (2020). On the loss mechanisms of radiation belt electron dropouts during the 12 September 2014 geomagnetic storm. *Earth and Planetary Physics*, 4(6), 598-610.
<https://agupubs.onlinelibrary.wiley.com/doi/abs/10.26464/epp2020060>
- Mann, I. R., & Ozeke, L. G. (2016). How quickly, how deeply, and how strongly can dynamical outer boundary conditions impact Van Allen radiation belt morphology? *Journal of Geophysical Research: Space Physics*, 121(6), 5553-5558.
<https://agupubs.onlinelibrary.wiley.com/doi/abs/10.1002/2016JA022647>
- McFadden, J. P., Carlson, C. W., Larson, D., Ludlam, M., Abiad, R., Elliott, B., et al. (2008). The THEMIS ESA Plasma Instrument and In-flight Calibration. *Space Science Reviews*, 141(1), 277-302.
<https://doi.org/10.1007/s11214-008-9440-2>
- Meredith, N. P., Thorne, R. M., Horne, R. B., Summers, D., Fraser, B. J., & Anderson, R. R. (2003). Statistical analysis of relativistic electron energies for cyclotron resonance with EMIC waves

- observed on CRRES. *Journal of Geophysical Research: Space Physics*, 108(A6).
<https://agupubs.onlinelibrary.wiley.com/doi/abs/10.1029/2002JA009700>
- Miyoshi, Y., Sakaguchi, K., Shiokawa, K., Evans, D., Albert, J., Connors, M., & Jordanova, V. (2008). Precipitation of radiation belt electrons by EMIC waves, observed from ground and space. *Geophysical Research Letters*, 35(23).
<https://agupubs.onlinelibrary.wiley.com/doi/abs/10.1029/2008GL035727>
- Morley, S. K., Friedel, R. H. W., Spanswick, E. L., Reeves, G. D., Steinberg, J. T., Koller, J., et al. (2010). Dropouts of the outer electron radiation belt in response to solar wind stream interfaces: Global positioning system observations. *Proceedings of the Royal Society A: Mathematical, Physical and Engineering Sciences*, 466(2123), 3329–3350.
- Nakamura, R., Isowa, M., Kamide, Y., Baker, D. N., Blake, J. B., & Looper, M. (2000). SAMPEX observations of precipitation bursts in the outer radiation belt. *Journal of Geophysical Research: Space Physics*, 105(A7), 15875–15885.
<https://agupubs.onlinelibrary.wiley.com/doi/abs/10.1029/2000JA900018>
- Ni, B., Cao, X., Zou, Z., Zhou, C., Gu, X., Bortnik, J., et al. (2015). Resonant scattering of outer zone relativistic electrons by multiband EMIC waves and resultant electron loss time scales. *Journal of Geophysical Research: Space Physics*, 120(9), 7357–7373.
<https://agupubs.onlinelibrary.wiley.com/doi/abs/10.1002/2015JA021466>
- Pierrard, V., Botek, E., Ripoll, J.-F., & Cunningham, G. (2020). Electron Dropout Events and Flux Enhancements Associated With Geomagnetic Storms Observed by PROBA-V/Energetic Particle Telescope From 2013 to 2019. *Journal of Geophysical Research: Space Physics*, 125(12), e2020JA028487.
<https://agupubs.onlinelibrary.wiley.com/doi/abs/10.1029/2020JA028487>
- Reeves, G. D., McAdams, K. L., Friedel, R. H. W., & O'Brien, T. P. (2003). Acceleration and loss of relativistic electrons during geomagnetic storms. *Geophysical Research Letters*, 30(10).
<https://agupubs.onlinelibrary.wiley.com/doi/abs/10.1029/2002GL016513>
- Ripoll, J.-F., Claudepierre, S. G., Ukhorskiy, A. Y., Colpitts, C., Li, X., Fennell, J. F., & Crabtree, C. (2020). Particle Dynamics in the Earth's Radiation Belts: Review of Current Research and Open Questions. *Journal of Geophysical Research: Space Physics*, 125(5), e2019JA026735.
<https://agupubs.onlinelibrary.wiley.com/doi/abs/10.1029/2019JA026735>
- Rodriguez, J. V. (2014a). *GOES 13–15 MAGE/PD pitch angles algorithm theoretical basis document*. Retrieved from
<https://ngdc.noaa.gov/stp/satellite/goes/documentation.html>.
- Rodriguez, J. V. (2014b). *GOES EPEAD science-quality electron fluxes algorithm theoretical basis document*. Retrieved from
https://ngdc.noaa.gov/stp/satellite/goes/doc/EPEAD_Electron_Science_Reprocessing_ATB_D_v1.0.pdf
- Scolini, C., Chané, E., Temmer, M., Kilpua, E. K. J., Dissauer, K., Veronig, A. M., et al. (2020). CME–CME Interactions as Sources of CME Geoeffectiveness: The Formation of the Complex

- 500 Ejecta and Intense Geomagnetic Storm in 2017 Early September. *The Astrophysical Journal*
501 *Supplement Series*, 247(1), 21. <http://dx.doi.org/10.3847/1538-4365/ab6216>
- 502 Selesnick, R. S., & Blake, J. B. (2000). On the source location of radiation belt relativistic electrons.
503 *Journal of Geophysical Research: Space Physics*, 105(A2), 2607-2624.
504 <https://agupubs.onlinelibrary.wiley.com/doi/abs/10.1029/1999JA900445>
- 505 Shen, C., Xu, M., Wang, Y., Chi, Y., & Luo, B. (2018). Why the Shock-ICME Complex Structure Is
506 Important: Learning from the Early 2017 September CMEs. *The Astrophysical Journal*,
507 861(1), 28. <http://dx.doi.org/10.3847/1538-4357/aac204>
- 508 Shprits, Y. Y., Horne, R. B., Kellerman, A. C., & Drozdov, A. Y. (2018). The dynamics of Van Allen
509 belts revisited. *Nature Physics*, 14(2), 102-103. <https://doi.org/10.1038/nphys4350>
- 510 Shprits, Y. Y., Kellerman, A., Aseev, N., Drozdov, A. Y., & Michaelis, I. (2017). Multi-MeV electron
511 loss in the heart of the radiation belts. *Geophysical Research Letters*, 44(3), 1204-1209.
512 <https://agupubs.onlinelibrary.wiley.com/doi/abs/10.1002/2016GL072258>
- 513 Shprits, Y. Y., Thorne, R. M., Friedel, R., Reeves, G. D., Fennell, J., Baker, D. N., & Kanekal, S. G. (2006).
514 Outward radial diffusion driven by losses at magnetopause. *Journal of Geophysical*
515 *Research: Space Physics*, 111(A11).
516 <https://agupubs.onlinelibrary.wiley.com/doi/abs/10.1029/2006JA011657>
- 517 Shue, J.-H., Song, P., Russell, C. T., Steinberg, J. T., Chao, J. K., Zastenker, G., et al. (1998).
518 Magnetopause location under extreme solar wind conditions. *Journal of Geophysical*
519 *Research: Space Physics*, 103(A8), 17691-17700.
520 <https://agupubs.onlinelibrary.wiley.com/doi/abs/10.1029/98JA01103>
- 521 Sillanpää, I., Ganushkina, N. Y., Dubyagin, S., & Rodriguez, J. V. (2017). Electron Fluxes at
522 Geostationary Orbit From GOES MAGED Data. *Space Weather*, 15(12), 1602-1614.
523 <https://agupubs.onlinelibrary.wiley.com/doi/abs/10.1002/2017SW001698>
- 524 Staples, F. A., Kellerman, A., Murphy, K. R., Rae, I. J., Sandhu, J. K., & Forsyth, C. (2022). Resolving
525 Magnetopause Shadowing Using Multimission Measurements of Phase Space Density.
526 *Journal of Geophysical Research: Space Physics*, 127(2), e2021JA029298.
527 <https://agupubs.onlinelibrary.wiley.com/doi/abs/10.1029/2021JA029298>
- 528 Summers, D., Ni, B., & Meredith, N. P. (2007). Timescales for radiation belt electron acceleration
529 and loss due to resonant wave-particle interactions: 2. Evaluation for VLF chorus, ELF hiss,
530 and electromagnetic ion cyclotron waves. *Journal of Geophysical Research: Space Physics*,
531 112(A4). <https://agupubs.onlinelibrary.wiley.com/doi/abs/10.1029/2006JA011993>
- 532 Thébaud, E., Finlay, C. C., Beggan, C. D., Alken, P., Aubert, J., Barrois, O., et al. (2015). International
533 Geomagnetic Reference Field: the 12th generation. *Earth, Planets and Space*, 67(1), 79.
534 <https://doi.org/10.1186/s40623-015-0228-9>
- 535 Thorne, R. M., & Kennel, C. F. (1971). Relativistic electron precipitation during magnetic storm main
536 phase. *Journal of Geophysical Research (1896-1977)*, 76(19), 4446-4453.
537 <https://agupubs.onlinelibrary.wiley.com/doi/abs/10.1029/JA076i019p04446>

- 538 Tsyganenko, N. A. (1989). A magnetospheric magnetic field model with a warped tail current sheet.
539 *Planetary and Space Science*, 37(1), 5-20.
540 <https://www.sciencedirect.com/science/article/pii/0032063389900664>
- 541 Turner, D. L., Angelopoulos, V., Morley, S. K., Henderson, M. G., Reeves, G. D., Li, W., et al. (2014).
542 On the cause and extent of outer radiation belt losses during the 30 September 2012
543 dropout event. *Journal of Geophysical Research: Space Physics*, 119(3), 1530-1540.
544 <https://agupubs.onlinelibrary.wiley.com/doi/abs/10.1002/2013JA019446>
- 545 Turner, D. L., Morley, S. K., Miyoshi, Y., Ni, B., & Huang, C.-L. (2012a). Outer Radiation Belt Flux
546 Dropouts: Current Understanding and Unresolved Questions. In *Dynamics of the Earth's*
547 *Radiation Belts and Inner Magnetosphere* (pp. 195-212).
- 548 Turner, D. L., Shprits, Y. Y., Hartinger, M. D., & Angelopoulos, V. (2012b). Explaining sudden losses
549 of outer radiation belt electrons during geomagnetic storms. *Nature Physics*, 8(3), 208-212.
550 <https://doi.org/10.1038/nphys2185>
- 551 Turner, D. L., & Ukhorskiy, A. Y. (2020). Chapter 1 - Outer radiation belt losses by magnetopause
552 incursions and outward radial transport: new insight and outstanding questions from the
553 Van Allen Probes era. In A. N. Jaynes & M. E. Usanova (Eds.), *The Dynamic Loss of Earth's*
554 *Radiation Belts* (pp. 1-28): Elsevier.
- 555 Tuszewski, M., Cayton, T. E., Ingraham, J. C., & Kippen, R. M. (2004). Bremsstrahlung effects in
556 energetic particle detectors. *Space Weather*, 2(10).
557 <https://agupubs.onlinelibrary.wiley.com/doi/abs/10.1029/2003SW000057>
- 558 Usanova, M. E., Drozdov, A., Orlova, K., Mann, I. R., Shprits, Y., Robertson, M. T., et al. (2014). Effect
559 of EMIC waves on relativistic and ultrarelativistic electron populations: Ground-based and
560 Van Allen Probes observations. *Geophysical Research Letters*, 41(5), 1375-1381.
561 <https://agupubs.onlinelibrary.wiley.com/doi/abs/10.1002/2013GL059024>
- 562 Usanova, M. E., Mann, I. R., Rae, I. J., Kale, Z. C., Angelopoulos, V., Bonnell, J. W., et al. (2008).
563 Multipoint observations of magnetospheric compression-related EMIC Pc1 waves by
564 THEMIS and CARISMA. *Geophysical Research Letters*, 35(17).
565 <https://agupubs.onlinelibrary.wiley.com/doi/abs/10.1029/2008GL034458>
- 566 Werner, A. L. E., Yordanova, E., Dimmock, A. P., & Temmer, M. (2019). Modeling the Multiple CME
567 Interaction Event on 6–9 September 2017 with WSA-ENLIL+Cone. *Space Weather*, 17(2),
568 357-369. <https://agupubs.onlinelibrary.wiley.com/doi/abs/10.1029/2018SW001993>
- 569 Xiang, Z., Tu, W., Li, X., Ni, B., Morley, S. K., & Baker, D. N. (2017). Understanding the Mechanisms
570 of Radiation Belt Dropouts Observed by Van Allen Probes. *Journal of Geophysical Research:*
571 *Space Physics*, 122(10), 9858-9879.
572 <https://agupubs.onlinelibrary.wiley.com/doi/abs/10.1002/2017JA024487>
- 573 Xiang, Z., Tu, W., Ni, B., Henderson, M. G., & Cao, X. (2018). A Statistical Survey of Radiation Belt
574 Dropouts Observed by Van Allen Probes. *Geophysical Research Letters*, 45(16), 8035-8043.
575 <https://agupubs.onlinelibrary.wiley.com/doi/abs/10.1029/2018GL078907>

Xue, Z., Yuan, Z., & Yu, X. (2021). Prompt Emergence and Disappearance of EMIC Waves Driven by the Sequentially Enhanced Solar Wind Dynamic Pressure. *Geophysical Research Letters*, 48(2), e2020GL091479. <https://agupubs.onlinelibrary.wiley.com/doi/abs/10.1029/2020GL091479>

Zhang, X.-J., Li, W., Ma, Q., Thorne, R. M., Angelopoulos, V., Bortnik, J., et al. (2016). Direct evidence for EMIC wave scattering of relativistic electrons in space. *Journal of Geophysical Research: Space Physics*, 121(7), 6620-6631. <https://agupubs.onlinelibrary.wiley.com/doi/abs/10.1002/2016JA022521>

Supporting Information References

Claudepierre, S. G., Ma, Q., & Bortnik, J. (2022). Quantifying Radiation Belt Electron Loss Processes at $L < 4$. *Journal of Geophysical Research: Space Physics*, 127(10), e2022JA030756. <https://agupubs.onlinelibrary.wiley.com/doi/abs/10.1029/2022JA030756>.